PAPER

Check for updates

Exploring the oxygen evolution electrocatalysis of an amine-based cobalt metal–organic framework†

Jade Nadine S. Ang, [ID] Manjunath Chatti, [ID] Khang N. Dinh, Stuart R. Batten, [ID] *
Alexandr N. Simonov [ID] * and David R. Turner [ID] *

When immobilised on a suitable electrode surface, metal organic frameworks (MOFs) can effectively promote the oxygen evolution reaction (OER) – the anode process of water electrolysis for the green hydrogen synthesis – most commonly through the electrooxidative decomposition of the framework into thermodynamically stable (oxy)hydroxides/oxides. In this study, the potential advantageous electrocatalytic effect of the macrocyclic amine core coordinating to the cobalt ions in an interdigitating 2D sheet framework is investigated. Nickel foam electrodes modified with **Co-TMBT-MOF** at a low loading of 0.25 mg cm^{-2} (0.004 mmol$_{Co}$ cm^{-2}) sustained the OER rate of 20 mA cm^{-2} (80 A g$_{MOF}^{-1}$) in 1 M KOH at ambient temperature at a stabilised overpotential of only 0.294 ± 0.005 V on a timescale of 20 h. Physical characterisation of the electrode after the OER tests confirmed transformation of the MOF into the catalytically active cobalt oxyhydroxide.

Design, System, Application

The system reported in this manuscript incorporates the molecular design of a strongly chelating ligand used as part of the metal–organic framework. In doing so, the stability of the material is greatly enhanced, preventing leaching of the metal and decomposition of the framework. This stability enables the material to be used and processed as an aqueous suspension. In the current study we demonstrate that this allows effective deposition on nickel foam as a pre-catalyst for the OER.

Introduction

As the demand for energy is rapidly exceeding the supply, the renewable energy research sector has been pulling out all the stops to find cleaner alternatives to fossil fuels. Electrochemical water splitting is one of the most widely studied routes to developing sustainable energy systems.[1–3] Practical water electrolysis requires the use of either acidic or alkaline electrolytes. The latter presents an important advantage of the improved stability of the device components without the need for use of noble metals and other highly expensive components, and is the focus herein.

While both cathode and anode half-reactions of the water electrolysis process require catalysts to achieve practical rates at economically feasible overpotentials, the oxygen evolution

reaction (OER) is a major contributor of the two to the energy efficiency losses.[4,5] Hence, a great variety of OER electrocatalysts continue to be developed using different combinations of transition metal (hydr)oxides/oxyhydroxides,[6–8] chalcogenides,[9–11] pnictides,[12–14] and their composites.[15–17]

Among different strategies to the design of OER catalysts, the use of metal–organic frameworks (MOFs), or porous coordination polymers (PCPs), has recently attracted some attention due to the very high internal surface area, tailorable pore size, ability to embed different functionalities, and the variety of metal nodes pertinent to MOFs.[18–22] Hypothetically, these characteristics give the potential for electrically conductive MOFs to present a very high concentration of catalytically active sites and rapid mass/charge transport rates as compared to the conventional bulk metal oxide derivatives.[23] However, it is highly unlikely for any MOF to maintain its structural integrity during the OER, even during model ambient temperature tests, due to an obvious thermodynamic instability of these materials under the very harsh conditions of a water splitting anode.[24] Indeed, it has been expectedly demonstrated that electrochemical testing of MOFs induces their transformation into corresponding

*School of Chemistry, Monash University, Clayton, VIC 3800, Australia.
E-mail: david.turner@monash.edu*

transition metal (hydr)oxides, which present the genuine catalytic species for the OER. Hence, the ability to produce a high-performance MOF-derived electrocatalyst will strongly depend on the initial stability of the MOF and its ability to preserve the initial texture with very high accessibility of the metal sites upon transformation into the oxide-based catalyst. Formation of catalysts in this way can give enhanced surface areas or different nanostructures than other methods.

To date, numerous transition metal-based MOFs, especially cobalt-based, have been used to produce electrodes with highly promising catalytic activity for the OER.[23,25–31] Some of the noteworthy results obtained at ambient temperature using a 1 M KOH electrolyte solution are surveyed here. Yu *et al.* used biphenyl-4,4′-dicarboxylic acid (H_2BPDC) to form Co-MOF nanosheets directly on a nickel foam (NF) electrode substrate using a hydrothermal method.[26] The 3D macroporous structure of the NF paired with the 2D Co-MOF nanosheets enabled the material to achieve the OER rate of 20 mA cm^{-2} (4.6 A g$_{MOF}^{-1}$) at an overpotential of *ca.* 0.29 V. Zhao *et al.* studied NiCo-MOF nanosheets using benzene-1,4-dicarboxylate as the organic ligand and suggested that the unsaturated metal surface atoms served as the dominant catalytic active centres of the OER.[32] However, their X-ray absorption data suggest that the NiCo-MOF was completely transformed into transition metal oxyhydroxides, which effectively catalysed the OER with the reaction rate of 10 mA cm^{-2} (50 A g$_{MOF}^{-1}$) achieved at an overpotential of *ca.* 0.25 V. Zhuang *et al.* used FeCo-MOF nanosheets with 1,3,5-benzenetricarboxylate as the ligand and observed a similar synergistic effect between Co and Fe.[33] Similarly, Tian *et al.* also formed a FeCo-MOF with nitrogen sites incorporated (as triazole) into the structure using 2,5-bis(1,2,4-triazol-1-yl)terephthalate ($BTTA^{2-}$) as the organic component. Their MOF-derived electrocatalyst displayed an OER rate of 10 mA cm^{-2} (20 A g$_{MOF}^{-1}$) at a very low overpotential of *ca.* 0.23 V. Their study also demonstrated the importance of using a highly conductive substrate like NF and doping with other metals for enhanced activity.[34]

Further insight into the usage of the different ligand components in MOF precatalysts should be explored to effectively utilise these materials. In this study, a ligand containing an amine-based macrocyclic core with biphenyl-carboxylate arms was designed to explore the functional advantage of having a metal chelating site in potentially enhancing stability (Fig. 1, bottom). The new **Co-TMBT-MOF** material was explored as a precursor for a cobalt-based oxygen evolution catalyst operating in alkaline electrolyte solutions.

Experimental

Materials

All starting materials were of ACS reagent grade and used as received from commercial suppliers (Alfa Aesar, Merck, Oakwood, and Sigma Aldrich) without further purification.

Fig. 1 Designed TACN-based tricarboxylic acid H$_3$**2** with extended, rigid arms compared to the previously reported H$_3$**1** (top), magnified view of the dinuclear Zn cluster in poly-[Zn$_2$(**2**)(OH$_2$)]Cl (middle), and view of the pore channels along the crystallographic *c*-axis (bottom).

1,4,7-Triazacyclononane trihydrochloride (TACN·3HCl) was synthesised using a previously reported literature procedure.[35] Ni foam (NF, >99.99%; thickness 1.6 mm; surface density 346 g m^{-2}; porosity ≥95%, 80–110 pores per inch) was obtained from Marketech International. Pt wire was purchased from A&E Metals. All solutions were prepared using ultrapure deionised water with resistivity of 18.2 MΩ cm at 23 °C derived from Sartorius Arium Comfort I

Ultrapure water system H$_2$O-I-1-UV-T; the same quality water was used for all procedures requiring H$_2$O.

Synthesis

Synthesis of 4′-methylbiphenyl-4-carboxylate. A Suzuki coupling reaction was performed using 4-methylbromobenzoate (4.000 g, 18.60 mmol), *p*-tolylboronic acid (2.530 g, 18.60 mmol), potassium carbonate (7.710 g, 55.80 mmol) and Pd(dppf)Cl$_2$ (455.7 mg, 558.0 μmol) as a catalyst in a tetrahydrofuran : H$_2$O (2 : 1 vol.) mixture at 70 °C for 24 hours under N$_2$. The reaction mixture was filtered through Celite under vacuum to remove the Pd catalyst. The filtrate was concentrated and the organic product was extracted into ethyl acetate after washing with distilled H$_2$O and brine. Purification was conducted using column chromatography with 10 : 90 to 20 : 80 vol. ethyl acetate in petroleum benzine (87% yield). ^{1}H NMR (400 MHz, CDCl$_3$) δ 8.09 (d, *J* = 8.4 Hz, 2H, ArH), 7.65 (d, *J* = 8.4 Hz, 2H, ArH), 7.53 (d, *J* = 8.1 Hz, 2H, ArH), 7.28 (d, *J* = 7.6 Hz, 2H, ArH), 3.94 (s, 3H, RCO$_2$–CH$_3$), 2.41 (s, 3H, ArCH$_3$).

Synthesis of 4′-bromomethyl-1,1′-biphenyl-4-carboxylate. Bromination of the pure 4′-methylbiphenyl-4-methylcarboxylate (3.659 g, 16.17 mmol) was conducted with *N*-bromosuccinimide (3.170 g, 17.79 mmol) and benzoyl peroxide (195.9 mg, 808.6 μmol) dissolved in dry acetonitrile (100 mL) under N$_2$ at 90 °C for 24 hours. Column chromatography using 10 : 90 to 20 : 80 vol. ethyl acetate in petroleum benzine was performed to purify the product (95% yield). ^{1}H NMR (400 MHz, CDCl$_3$) δ 8.11 (d, *J* = 8.7 Hz, 2H, ArH), 7.65 (d, *J* = 8.6 Hz, 2H, ArH), 7.60 (d, *J* = 8.3 Hz, 2H, ArH), 7.49 (d, *J* = 8.3 Hz, 2H, ArH), 4.55 (s, 2H, BrCH$_2$), 3.94 (s, 3H, RCO$_2$–CH$_3$).

Synthesis of 1,4,7-tris(4′-methylbiphenyl-4-carboxylic)-1,4,7-triazacyclononane hydrochloride salt dihydrate, H$_3$2·3HCl·2H$_2$O. The pure brominated ester (4.691 g, 15.37 mmol) was mixed with TACN·3HCl (1.180 g, 4.960 mmol) and K$_2$CO$_3$ (6.170 g, 44.63 mmol) in acetonitrile (100 mL) at 90 °C for 24 hours. The reaction mixture was filtered and the resulting precipitate (3.338 g, 4.160 mmol) contained the desired product which was subsequently demethylated with potassium hydroxide (1.400 g, 24.98 mmol) in tetrahydrofuran : H$_2$O (60 mL, 1 : 2 vol.) for 48 hours at 100 °C and rendered acidic (pH 3) with concentrated HCl. The product precipitated out of the solution and was recovered by filtration (2.068 g, 65% yield). ^{1}H NMR (600 MHz, DMSO-d$_6$) δ 7.96 (m, 6H, ArH), 7.67 (m, 12H, ArH), 7.29 (d, *J* = 7.8 Hz, 6H, ArH), 3.92 (s, 6H, R$_2$N–CH$_2$), 2.89 (s, 12H, TACN–CH$_2$). ^{13}C NMR (151 MHz, DMSO-d$_6$): δ 167.04, 143.48, 138.70, 130.56, 129.96, 127.09, 126.64, 118.93, 72.20, 57.03, 44.46, 39.94, 39.80, 39.66, 39.52, 39.38, 39.24, 39.10. *m/z* (ES+): 760.33 ([M + H]$^+$ 53.0%, calculated for C$_{48}$H$_{46}$N$_3$O$_6$$^+$, MW = 760.33. FTIR ($v$/cm^{-1}): 3405 m, 2954w, 2886w, 2814m, 2499w, 2113w, 1794w, 1702s, 1607s, 1396s, 1272s, 1107s, 1006m, 958m, 821m, 770s, 754s, 698s. Found: C, 63.60; H, 5.34; N, 4.68%; calculated for C$_{48}$H$_{45}$N$_3$O$_6$·3HCl·2H$_2$O: C, 63.68; H, 5.79; N, 4.64%.

Synthesis of poly-[Co(H2)(OH$_2$)]·2DMF·4H$_2$O, Co-TMBT-MOF. H$_3$2·3HCl·2H$_2$O (0.0100 g, 13.2 μmol) was mixed with four

equivalents of Co(NO$_3$)$_2$·6H$_2$O (0.0153 g, 52.6 μmol) in a vial containing *N,N*-dimethylformamide (2 mL), H$_2$O (0.2 mL), and acetic acid (0.1 mL). The mixture was sonicated and placed into a dry incubator set at 90 °C. Purple crystals formed at the bottom of the vial after 7 days. FTIR (v/cm^{-1}): 2907w, 2322w, 2112w, 1994w, 1905w, 1803w, 1707m, 1658m, 1591s, 1382s, 1238m, 1084s, 975m, 781s, 704s, 653s. TGA: 30–125 °C, mass loss = 19% (calculated 20% for 2 DMF and 3 H$_2$O). The sample started to decompose at 300 °C. Found: C, 58.19; H, 6.12; N, 6.41%; calculated for poly-[Co(H2)(OH$_2$)]·2DMF·7H$_2$O: C, 58.58; H, 6.65; N, 6.33%. Bulk purity of the crystalline material was confirmed by PXRD (see Fig. S4a†). TGA and elemental analysis are in reasonable agreement with calculations from the Olex2 solvent mask routine on the single crystal data of poly-[Co(H2)(OH$_2$)]·DMF·H$_2$O which found an additional 72 e$^-$ per formula unit (DMF·3H$_2$O = 70 e$^-$).

Synthesis of poly-[Zn$_2$(2)(OH$_2$)]Cl·2.5DMF·6.5H$_2$O, Zn-TMBT-MOF. 4.5 equivalents of Zn(NO$_3$)$_2$·6H$_2$O (0.0176 g, 73.8 μmol) was added to **H$_3$2·3HCl·2H$_2$O** (0.0100 g, 13.2 μmol) in a vial containing a mixture of *N,N*-dimethylformamide (2 mL), H$_2$O (0.2 mL), and acetic acid (0.1 mL). The vial was sonicated and placed into a dry bath incubator set at 90 °C. Tiny faint yellow cubic crystals formed on the vial wall after a day. FTIR (v/cm^{-1}): 2863w, 2300w, 1995w, 1655m, 1605m, 1529w, 1492w, 1389s, 1209m, 1088s, 978m, 821m, 784s, 706m, 655m. TGA: 30–96 °C, mass loss = 6% (calculated 26% for 2.5 DMF and 7.5 H$_2$O; 6% for 3 H$_2$O). The sample started to decompose at 380 °C. Found: C, 53.91; H, 5.52; N, 5.47%; calculated for poly-[Zn$_2$(2)(OH$_2$)]Cl·1.5DMF·6.5H$_2$O: C, 54.00; H, 5.83; N, 5.40%. Some solvent loss is assumed to have occurred prior to analysis by both TGA and elemental analysis. Bulk purity of the crystalline material was confirmed by PXRD (see Fig. S4b†). The Olex2 solvent mask routine suggests electron density equating to 180 e$^-$ per formula unit (calc. for Cl·2.5DMF·6.5H$_2$O = 182 e$^-$).

Materials characterisation

^{1}H and ^{13}C NMR spectroscopy. ^{1}H and ^{13}C NMR spectra were recorded at 298 K using either a Bruker Avance III nanobay NMR spectrometer equipped with a 9.4 T magnet and 5 mm BBFO probe, operating at 400.20 MHz (^{1}H) and 100.64 MHz (^{13}C), or a Bruker Avance III spectrometer equipped with a 14.1 T magnet and 5 mm TCI cryoprobe, operating at 600.27 MHz (^{1}H) and 150.95 MHz (^{13}C). High resolution mass spectrometry was performed using a Micromass Platform II QMS Electrospray Mass Spectrometer. Elemental microanalyses for C, H, and N were obtained from a 2400 Series II CHNS/O Analyser. Thermogravimetric analyses (TGA) were conducted using a Mettler Toledo TGA/DSC1 STARe system with a temperature ramping rate of 3 °C min^{-1} from 25–500 °C under a N$_2$ atmosphere. IR spectra were taken using an Agilent Cary 630 Fourier transform infrared (FTIR) spectrometer with the diamond attenuated total reflection (ATR) setup.

Single crystal X-ray diffraction (SC-XRD). SC-XRD data were collected using either the Rigaku SynergyS

diffractometer (Cu-Kα source, 1.54184 Å, 123 K), or the MX2 beamline at the Australian Synchrotron (17.4 keV, 0.7108 Å, 100 K).[36,37] Data collection at the Australian Synchrotron was performed using the in-house control systems while data reduction and integration were completed using the XDS software suite.[38] Control and processing for Rigaku data used the CrysAlisPro software package. Both crystal structures were solved using SHELXT[39] and refined against F^2 by full matrix least-squares procedures using SHELXL-2018[40] within Olex2.[41] Anisotropic displacement parameters were used to refine non-hydrogen atoms. Hydrogen atoms were assigned to calculated positions with isotropic displacement parameters 1.2 or 1.5 times their carrier atoms. The Solvent Mask routine in Olex2 was used to account for the electron density within voids that could not be sensibly modelled (see ESI† for crystallographic and refinement parameters and special refinement details).[42] Data are deposited with the CCDC.

Powder X-ray diffraction (PXRD). PXRD analysis was conducted using a Bruker D8 Advance Eco diffractometer with a Cu-Kα radiation source. Samples were mounted on a zero-background silicon single crystal stage and scanned at 2-theta angles of 5 to 55° with a step size of 0.02 using the Bragg–Brentano parafocusing geometry. All PXRD data were collected at 298 K and were compared against calculated patterns from the low temperature SC-XRD data.

X-ray photoelectron spectroscopy (XPS). XPS data were recorded using a Thermo Scientific Nexsa Surface Analysis System equipped with a hemispherical analyser and a monochromatic radiation source, Al-Kα X-rays (1486.6 eV) at 72 W (6 mA and 12 kV, 400 × 800 μm² spot). Charge neutralisation *via* a low-energy dual-beam (ion and electron) flood source was used. The pass energy, voltage step size and dwell time were 200 eV, 1 eV and 10 ms for the survey scans, respectively, whereas for the high-resolution scans these parameters were 50 eV, 0.1 eV and 50 ms. This produced a full-width at half of the maximum of 0.86–0.87 eV for the Ag $3d_{5/2}$ peak and <1.0 eV for the ester peak in PET during performance tests. Sampling depth may range from 0 to *ca.* 10 nm as the actual emission angle is ill-defined due to the rough surfaces present (ranging from 0° to 90°). Data were processed using Thermo Avantage v5.9902 with the energy calibration referenced to the aliphatic C 1s peak at 284.8 eV. Two different spots per sample were surveyed to ensure the consistency of the results.

Inductively coupled plasma mass-spectrometry (ICP-MS). ICP-MS analysis was performed using a Perkin Elmer NexION 2000 instrument on the used electrolyte solutions. Calibration curves were constructed using systematic dilutions of commercial stock solutions to concentrations of 0.01–50 μg mL^{-1} in 2 wt% HNO$_3$. The background was measured for each analysis using blank solutions prepared with 2 wt% HNO$_3$.

Scanning electron microscopic (SEM) and energy dispersive X-ray spectroscopy (EDS). SEM and EDS analysis was undertaken with a FEI Magellan-FEG instrument equipped with a Bruker Quantax silicon drift X-ray detector. Samples were dispersed in isopropanol and drop-cast onto a silicon slide, which was attached using a carbon tape and electrically connected with a copper tape to the aluminium SEM stub.

Electrochemical measurements

Electrochemical analysis was undertaken in a three-electrode configuration using an H-cell with the working and auxiliary compartments separated by a low-porosity (P4) ceramic frit and a Bio-Logic VSP electrochemical workstation at ambient temperature (23 ± 2 °C). Aqueous 1 M KOH electrolyte solution was saturated with O$_2$ in the working electrode compartment.

Working electrodes were prepared using Ni foam substrates with an active geometric area of 0.5 cm × 0.5 cm, which were cleaned by sonicating in concentrated HCl (*ca.* 32 wt%), rinsed and sonicated again in water and then in ethanol for 10 min each media. The working electrodes were dried overnight in a desiccator prior to use. The MOFs were deposited by drop-casting a suspension onto the NF working electrode substrates. The suspension was prepared using 5 mg of **Co-TMBT-MOF**, 50 μL of 5 wt% Nafion (ethanol solution), 250 μL of isopropanol, and 700 μL of water. The mixture was uniformly dispersed by sonication (Elmasonic E-60H 6-Quart bath) for 30 min before it was drop-cast onto the substrates. Loading levels were varied from 0.10 to 1.00 mg cm^{-2} (Fig. S5†).

A high surface area Pt wire was used as an auxiliary electrode. The Hg|HgO|1 M KOH reference electrode was confined in a glass tube with a P4 ceramic frit. All the potentials reported were converted to the reversible hydrogen electrode (RHE) scale using the experimentally measured potential of the reference electrode against the custom-made RHE[8] filled with 1 M KOH. Uncompensated resistance (R_u) was calculated from the electrochemical impedance spectra, which were collected at potentials where negligible faradaic processes were present, before and after experiments in a frequency range 200 kHz to 0.1 Hz at an amplitude 0.010 V. Typical R_u values were 0.3–0.4 Ω. Correction for the ohmic losses was done manually post-analysis by subtracting the IR_u product. All current densities are reported normalised to the geometric surface area of the electrodes or the amount of the catalytically relevant material.

Results and discussion

MOF synthesis and structure

A previously reported tris-benzylcarboxylic acid TACN ligand, H$_3$**1** (Fig. 1), forms a Zn-MOF, poly-[Zn$_2$(**1**)(H$_2$O)]Cl, which was used for CO$_2$ adsorption due to its porosity and rigidity.[43] Building on this design strategy, in which a central TACN pocket is able to tightly bind a transition metal and yet the structure still provides accessible pore space, a longer derivative using 4′-methylbiphenyl-4-carboxylic acid arms,

This journal is © The Royal Society of Chemistry and IChemE 2023

Mol. Syst. Des. Eng., 2023, **8**, 1004–1012 | 1007

H$_3$**2**, was synthesised in order to increase the pore space to provide easier access to the metal sites.

Initially, we were able to obtain faint yellow crystals of poly-[Zn$_2$(**2**)(OH$_2$)]Cl·1.5DMF·6.5H$_2$O, **Zn-TMBT-MOF**, directly from the heated reaction (see Experimental). The MOF is a 3D framework based on a dinuclear cluster (Fig. 1). Zn1 is coordinated to the three nitrogen atoms of the TACN core and to three carboxylate oxygen atoms. Zn2 is disordered over two sites and tetracoordinated to three carboxylate oxygen atoms as well as an aqua ligand. Each **2** ligand is coordinated to four Zn$_2$ clusters (one *via* the TACN ring and three *via* the carboxylates), and in turn each Zn$_2$ cluster is coordinated to four **2** ligands – three by carboxylate groups which generate a Zn$_2$(μ_2-CO$_2$)$_3$ motif, and one by the TACN group. This generates two interpenetrating 3D nets; if the nodes are defined as the **2** ligand and the Zn$_2$ clusters then a uninodal 4-connected (6^5·8) net of unusual topology is generated. Alternatively, if the Zn$_2$(CO$_2$)$_3$(TACN) moiety is considered as a node, then it can be described as a 6-connected 3^2·4^4·5^6·6^2·7 net.

The structure contains solvent-filled 1D channels equivalent to 48% of the crystal volume. A pore diameter of approximately 6 Å measured between the shortest C···C distance (including van der Waals radii) exists along the crystallographic *c*-axis (Fig. 1). The degree of solvation was assigned through chemical analysis, and the presence of the chloride counter-anion inferred from microanalysis and the analogous nature of the framework to those previously reported. Although this 3D Zn framework displays remarkable unrestricted pore channel accessibility, this study will focus on the **Co-TMBT-MOF** material, below, as cobalt-based compounds are well known to be good OER catalysts.

The 2D **Co-TMBT-MOF** adopts a very different structure to the zinc material, surprisingly considering the nature of the metals involved, with a purple crystalline material isolated directly from the reaction (see Experimental). SC-XRD shows the formation of poly-[Co(H**2**)(OH$_2$)]·2DMF·4H$_2$O as parallel interdigitated 2D sheets (Fig. 2). Each ligand coordinates to three metal ions, one through the TACN ring, and two others through the carboxylate arms. The third arm of each ligand remains protonated and uncoordinated; these arms project outwards on either side of the plane of the sheet. Each metal ion, which exists as a single ion node rather than the binuclear node in the Zn-MOF, coordinates to three ligands, one through the TACN ring, and two others through the carboxylate arms (there is also an additional water ligand). Thus, if one considers the metal and the ligand as 3-connecting nodes, the sheet has (6,3) topology (with both nodes topologically identical). However, it is perhaps better to consider a Co(H**2**)(OH$_2$) moiety as the node, where the Co is bound to the TACN ring of the ligand, in which case each node is connected to four others and the topology is (4,4) (Fig. 2 middle). As expected from the design strategy, the secondary amines of the core group holding the metal in
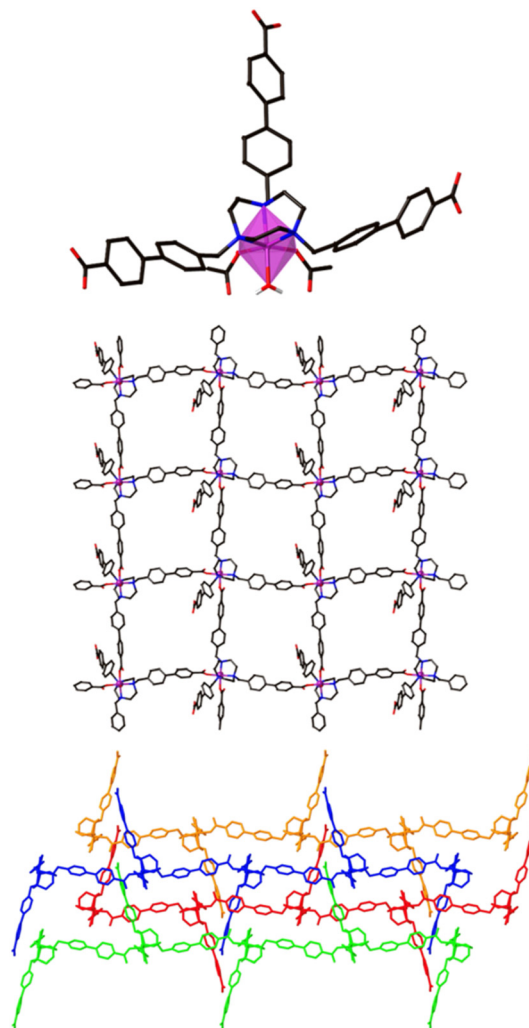

Fig. 2 Magnified view of the hexacoordinated Co node in the structure of poly-[Co$_2$(H**2**)(OH$_2$)]·2DMF·4H$_2$O (top), simplified view of the framework viewed along the crystallographic *a*-axis (middle), and an expanded view to highlight how the sheets stack with interdigitation in the *x* direction (bottom).

place providing extra stability for the framework, as evidenced by its stability in air after filtering and leaving exposed to the atmosphere for 24 h before determining its PXRD pattern (Fig. S4a†).

The sheets stack in the *x* direction and are highly interdigitated (Fig. 2 bottom), with the uncoordinated carboxylic acid arm of each ligand penetrating a window in each of two adjoining sheets and forming a hydrogen bond with the non-coordinated atom of a monodentate carboxylate of the sheet that is three removed. Each window in a sheet is in turn penetrated by two of these uncoordinated ligand arms, one from each of two adjoining sheets which lie on the same side of the original sheet. The interdigitation is such that all the windows in one row are penetrated by sheets from one side, while all the windows in the next row are penetrated by sheets from the other side. Even with this interdigitation, 1D channels exist parallel to the crystallographic *a* axis in which solvent

1008 | *Mol. Syst. Des. Eng.*, 2023, **8**, 1004–1012

This journal is © The Royal Society of Chemistry and IChemE 2023

molecules reside which could not be resolved from the single crystal X-ray diffraction data.

Electrocatalytic activity

Electrocatalytic oxygen evolution activity of the nickel foam electrodes modified with as synthesised **Co-TMBT-MOF** was investigated in 1 M KOH electrolyte solution at ambient temperature. During the cyclic voltammetry measurements (Fig. S6a†), the performance of **Co-TMBT-MOF**/NF improved with cycling suggesting an *in situ* chemical and structural transformation until stabilisation after *ca.* 10 cycles at 0.005 V s^{-1}. This transformation is most likely associated with the electrochemical oxidation of the metal organic species, which eventually leads to the formation of more catalytically active cobalt oxyhydroxide species. The highest performance was achieved at the initial MOF loading of 0.25 mg cm^{-2}, suggesting that higher amounts of the material limit the charge transport. Importantly, the background performance of the Ni foam substrate was negligibly low as compared to the MOF-modified electrodes in the investigated potential range (Fig. 3a).

Upon stabilisation of the voltammetric response, the electrocatalytic activity of the **Co-TMBT-MOF**/NF electrodes was investigated by short-term galvanostatic measurements (Fig. S6b†), which were used to construct an OER polarisation plot (Fig. 3b). The potential dependence of the current density was close to linear within the 20–80 mA cm^{-2} range indicating insignificant charge-transport limitations within the catalyst (Fig. S6b†). The corresponding Tafel slope was 0.053 ± 0.005 V dec^{-1}.

When tested in galvanostatic mode on a longer timescale, the **Co-TMBT-MOF**/NF electrodes exhibited even further improvements in the catalytic performance (Fig. 3c). Eventually, the quasi-steady state was achieved after *ca.* 5 h of operation at 20 mA cm^{-2}, which required only 0.294 ± 0.005 V overpotential, and the performance did not change further indicating that chemical transformations of **Co-TMBT-MOF** are complete at this stage. The electrocatalytic performance of these electrodes was highly reproducible, as confirmed through tests of three independent MOF samples (Fig. 3b and c and S6b and c†).

Comparisons of the OER performance reported herein to those of the recently reported Co-MOF-derived catalysts indicates that **Co-TMBT-MOF**/NF is among the top-performing electrodes of this class (Table S1†). The only material outperforming **Co-TMBT-MOF**/NF was derived from the FeCo-BTTA-MOF,[23] confirming the well-known promoting effect of iron on the OER activity. It should be also noted though that no measures were taken herein to purify the electrolyte solutions from the Fe impurities, meaning that the **Co-TMBT-MOF**/NF electrodes were likely modified with very low amounts of iron-based species, although they could not be detected by XPS (*vide infra*). Overall, the **Co-TMBT-MOF**/NF electrode with the MOF loading of 0.25 mg cm^{-2} (0.004 mmol$_{Co}$ cm^{-2}) maintained an OER rate of 20 mA cm^{-2} (80 A g$_{MOF}^{-1}$ or 4.5 A g$_{Co}^{-1}$) at a low overpotential of 0.294 ± 0.005 V.
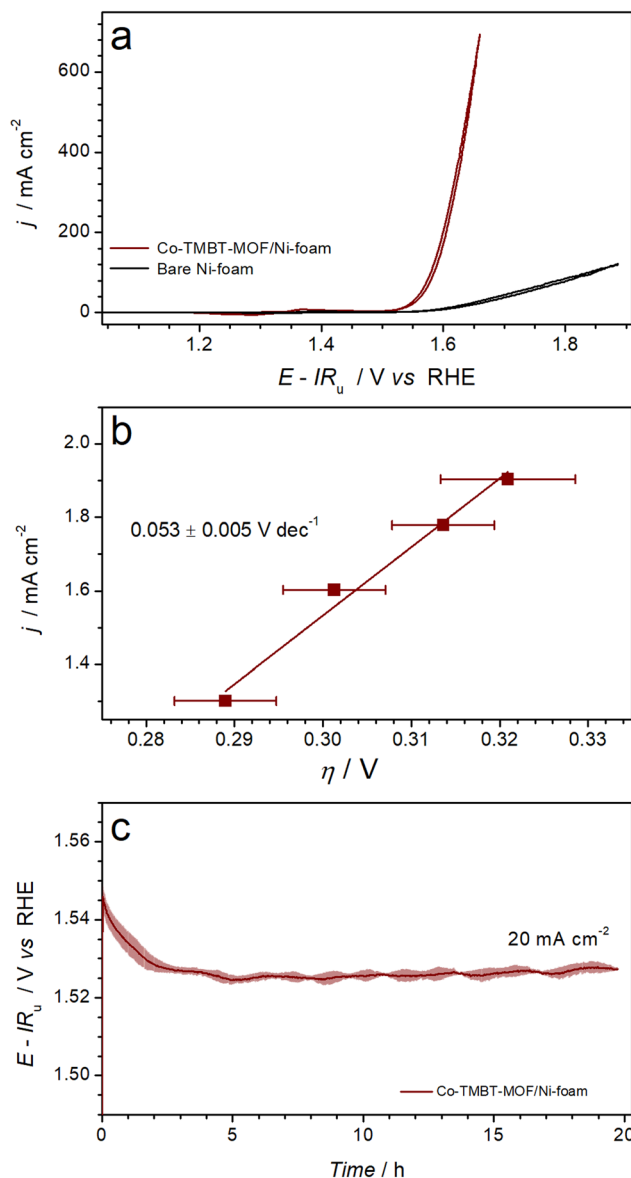
Fig. 3 Electrocatalytic OER performance of Ni foam electrodes modified with **Co-TMBT-MOF** (0.25 mg cm^{-2}) in 1 M KOH at 23 ± 2 °C: (a) quasi-stabilised cyclic voltammetry (scan rate 0.005 V s^{-1}; 10th scans) with black curve showing background data for the unmodified Ni foam electrode, (b) OER polarisation plots derived from potentiometric measurements (Fig. S6b†), and (c) longer-term galvanostatic OER at 20 mA cm^{-2}. Data in panels b and c are shown as mean (symbols and solid line) ± standard deviation (error bars and shading) derived from tests of three independent samples.

This activity is notably higher than that reported for CoOOH on NF, which required an overpotential of 0.37 ± 0.01 V at 10 mA cm^{-2} in 1 M KOH.[44,45]

Electrode characterisation

The **Co-TMBT-MOF**/NF electrodes were characterised before and after 20 h long OER tests at 20 mA cm^{-2} to ascertain the origin of the high electrocatalytic activity. The X-ray diffraction peaks for **Co-TMBT-MOF** and products of its

This journal is © The Royal Society of Chemistry and IChemE 2023

Mol. Syst. Des. Eng., 2023, **8**, 1004–1012 | **1009**

transformations cannot be unambiguously detected from the assembled electrode due to the low mass loading (Fig. S4b†). SEM images before the electrochemical measurements showed deposition of well-defined **Co-TMBT-MOF** grains with approximately 10 μm length and 2 μm width onto the NF substrate (Fig. 4a). After the OER tests, these small grains were transformed into larger sheet-like microstructures with the size of *ca.* 20–30 μm (Fig. 4b), as well as smaller grain-like nanostructures with the dimensions of a few hundred nanometres (Fig. 4c). The EDS mapping of the electrodes after the OER tests confirmed the presence of Co, as well as, quite unexpectedly, of N (Fig. S6†). Apparently, the duration of the tests used herein was insufficient for a complete elimination of the ligand from the electrode surface.
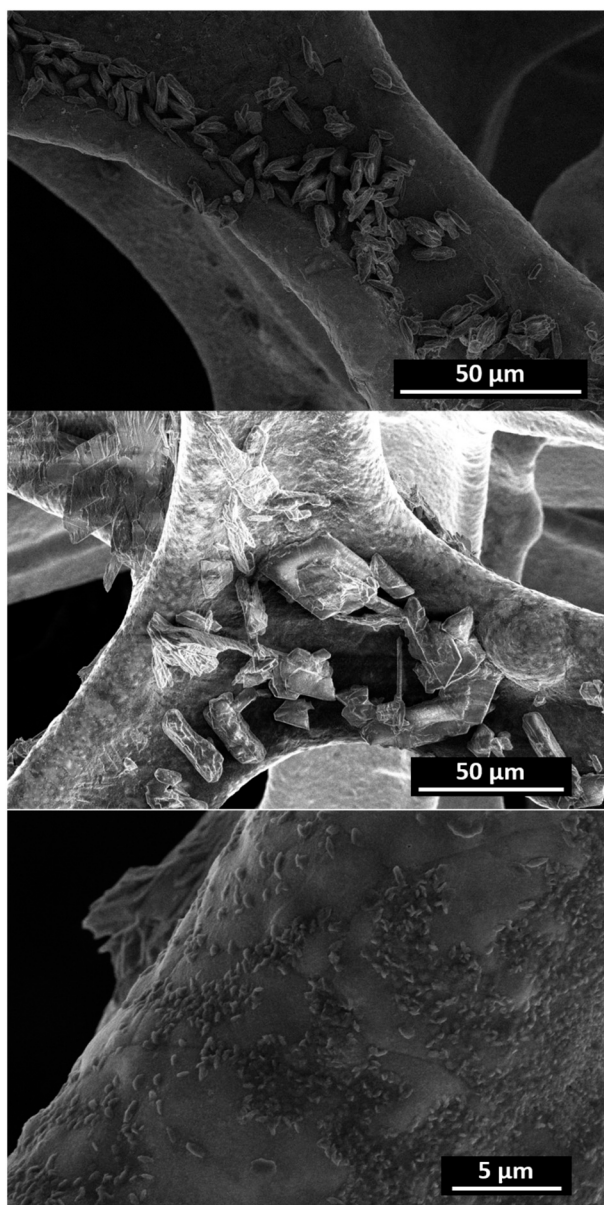

Fig. 5 High-resolution Co 2p XP spectra of the **Co-TMBT-MOF**/NF electrodes before and after the 20 h OER tests in 1 M KOH at 20 mA cm^{-2} and 23 ± 2 °C.

XPS analysis was used to establish the chemical nature of the observed morphological changes. The C 1s and N 1s spectra suggest decomposition and possible dissolution of the organic ligand from the metal centre, as concluded from the significant decrease of the O–C=O (288.6 eV) C 1s peak (Fig. S9b†) and the disappearance of the C–N (402.5 eV) and M–N (399.6 eV) N 1s signals (Fig. S9c†) after the OER tests. The presence of aliphatic C–OH on the surface of the as-prepared **Co-TMBT-MOF**/NF electrode is corroborated by a broad peak at 532.7 eV in the O 1s spectra, whereas much narrower O 1s signals shifted towards the lower binding energies typical of metal hydroxides[23,46,47] were recorded for the tested electrode. Notable changes were also induced to the Co 2p spectra. Notwithstanding the low signal-to-noise ratio associated with the low concentration of Co on the electrode surface, the change of the initial spectra, likely dominated by the Co^{2+} species,[48,49] to a set of signals typical of cobalt oxyhydroxide was detected (Fig. 5).[23,50,51] These have been referenced against existing literature of characterised standards of Co materials.[50] FTIR spectra of the electrode after the OER also showed a significant decrease in the intensity of the characteristic peaks of **Co-TMBT-MOF** confirming its electrochemically induced decomposition (Fig. S9†).

ICP-MS of the electrolyte solution after 20 h of the OER (20 mA cm^{-2}) catalysed by **Co-TMBT-MOF**/NF electrodes detected the presence 0.01 μM of Co which is equivalent to 0.07 mol% of the amount of cobalt initially deposited onto the electrode in the form of the MOF. The low amount of Co ions released after the activation is indicative of the electrochemical stability of the MOF-derived catalyst.

Conclusions

Crystal engineering plays an important role in ensuring that MOFs are rationally designed towards their targeted applications. The synthesised two-fold 2D sheet framework of poly-[Co$_2$(H2)(OH$_2$)]·2DMF·4H$_2$O, **Co-TMBT-MOF**, provides a strong chelating TACN core for Co. The assembled **Co-TMBT-**

Fig. 4 SEM images of **Co-TMBT-MOF**/NF before (top) and after the 20 h (centre and bottom) OER tests in 1 M KOH at 20 mA cm^{-2} and 23 ± 2 °C.

1010 | *Mol. Syst. Des. Eng.*, 2023, **8**, 1004–1012

This journal is © The Royal Society of Chemistry and IChemE 2023

MOF/NF electrode demonstrated a lower OER overpotential of 0.294 ± 0.005 V at a lower mass loading (0.25 mg cm^{-2}) than most of the reported Co-MOF derived catalysts. Durability tests show promising electrochemical stability with no decay for at least 20 h. Further investigation into the origin of the OER activity of the assembled electrode has shown that the chemical and structural transformation of the MOF into metal hydroxides and oxyhydroxides gives the primary active species for the OER.[52] This study helps confirm the usability of Co-MOFs as pre-catalysts regardless of them undergoing certain transformations as the electrochemical stability proves to be far more important for this application.

Author contributions

Conceptualisation, JNSA/MC/ANS/SRB/DRT; investigation, JNSA/MC/KND; writing – original draft, JNSA; writing – review & editing, JNSA/MC/KND/SRB/ANS/DRT.

Conflicts of interest

There are no conflicts to declare.

Acknowledgements

Notes and references

1 J. R. Rostrup-Nielsen, *Catal. Rev.: Sci. Eng.*, 2004, **46**, 247–270.

2 X. Li, X. Hao, A. Abudula and G. Guan, *J. Mater. Chem. A*, 2016, **4**, 11973–12000.

3 D. R. MacFarlane, J. Choi, B. H. R. Suryanto, R. Jalili, M. Chatti, L. M. Azofra and A. N. Simonov, *Adv. Mater.*, 2020, **32**, 1904804.

4 V. R. Stamenkovic, D. Strmcnik, P. P. Lopes and N. M. Markovic, *Nat. Mater.*, 2016, **16**, 57–69.

5 N.-T. Suen, S.-F. Hung, Q. Quan, N. Zhang, Y.-J. Xu and H. M. Chen, *Chem. Soc. Rev.*, 2017, **46**, 337–365.

6 P. W. Menezes, A. Indra, A. Bergmann, P. Chernev, C. Walter, H. Dau, P. Strasser and M. Driess, *J. Mater. Chem. A*, 2016, **4**, 10014–10022.

7 M. Chatti, A. M. Glushenkov, T. Gengenbach, G. P. Knowles, T. C. Mendes, A. V. Ellis, L. Spiccia, R. K. Hocking and A. N. Simonov, *Sustainable Energy Fuels*, 2018, **2**, 1561–1573.

8 D. Simondson, M. Chatti, S. A. Bonke, M. F. Tesch, R. Golnak, J. Xiao, D. A. Hoogeveen, P. V. Cherepanov, J. L. Gardiner, A. Tricoli, D. R. MacFarlane and A. N. Simonov, *Angew. Chem., Int. Ed.*, 2021, **60**, 15821–15826.

9 I. H. Kwak, H. S. Im, D. M. Jang, Y. W. Kim, K. Park, Y. R. Lim, E. H. Cha and J. Park, *ACS Appl. Mater. Interfaces*, 2016, **8**, 5327–5334.

10 W. Chen, Y. Liu, Y. Li, J. Sun, Y. Qiu, C. Liu, G. Zhou and Y. Cui, *Nano Lett.*, 2016, **16**, 7588–7596.

11 J.-H. Kim, K. Kawashima, B. R. Wygant, O. Mabayoje, Y. Liu, J. H. Wang and C. B. Mullins, *ACS Appl. Energy Mater.*, 2018, **1**, 5145–5150.

12 L.-A. Stern, L. Feng, F. Song and X. Hu, *Energy Environ. Sci.*, 2015, **8**, 2347–2351.

13 A. Dutta, A. K. Samantara, S. K. Dutta, B. K. Jena and N. Pradhan, *ACS Energy Lett.*, 2016, **1**, 169–174.

14 F. Yu, H. Zhou, Z. Zhu, J. Sun, R. He, J. Bao, S. Chen and Z. Ren, *ACS Catal.*, 2017, **7**, 2052–2057.

15 X. Zou, J. Su, R. Silva, A. Goswami, B. R. Sathe and T. Asefa, *Chem. Commun.*, 2013, **49**, 7522–7524.

16 X. Yu, M. Zhang, W. Yuan and G. Shi, *J. Mater. Chem. A*, 2015, **3**, 6921–6928.

17 H. Chen, Y. Gao, L. Ye, Y. Yao, X. Chen, Y. Wei and L. Sun, *Chem. Commun.*, 2018, **54**, 4979–4982.

18 G. R. Desiraju, J. J. Vittal and A. Ramanan, *Crystal Engineering: A Text Book*, World Scientific, 2011.

19 Y. Gong, H.-F. Shi, P.-G. Jiang, W. Hua and J.-H. Lin, *Cryst. Growth Des.*, 2014, **14**, 649–657.

20 J. Duan, S. Chen and C. Zhao, *Nat. Commun.*, 2017, **8**, 15341.

21 X. Zhao, B. Pattengale, D. Fan, Z. Zou, Y. Zhao, J. Du, J. Huang and C. Xu, *ACS Energy Lett.*, 2018, **3**, 2520–2526.

22 S. A. Patil, N. K. Shrestha, A. I. Inamdar, C. Bathula, J. Jung, S. Hussain, G. Nazir, M. Kaseem, H. Im and H. Kim, *Nanomaterials*, 2022, **12**, 1916.

23 J. Tian, F. Jiang, D. Yuan, L. Zhang, Q. Chen and M. Hong, *Angew. Chem., Int. Ed.*, 2020, **59**, 13101–13108.

24 E. A. Flügel, V. W.-H. Lau, H. Schlomberg, R. Glaum and B. V. Lotsch, *Chem. – Eur. J.*, 2016, **22**, 3676–3680.

25 K. Ge, S. Sun, Y. Zhao, K. Yang, S. Wang, Z. Zhang, J. Cao, Y. Yang, Y. Zhang, M. Pan and L. Zhu, *Angew. Chem., Int. Ed.*, 2021, **60**, 12097–12102.

26 J. Yu, Y. Cao, Q. Liu, Y. Luo, Y. Liu, X. Shi, A. M. Asiri, T. Li and X. Sun, *ChemNanoMat*, 2021, **7**, 906–909.

27 R. K. Tripathy, A. K. Samantara and J. N. Behera, *Dalton Trans.*, 2019, **48**, 10557–10564.

28 Q. Qian, Y. Li, Y. Liu, L. Yu and G. Zhang, *Adv. Mater.*, 2019, **31**, 1901139.

29 S. Ibrahim, I. Majeed, E. Hussain, A. Badshah, Y. Qian, D. Zhao, D. R. Turner and M. A. Nadeem, *Inorg. Chim. Acta*, 2019, **486**, 684–693.

30 S. Ibrahim, K. Shehzadi, B. Iqbal, S. Abbas, D. R. Turner and M. A. Nadeem, *J. Colloid Interface Sci.*, 2019, **545**, 269–275.

31 S. Li, Y. Gao, N. Li, L. Ge, X. Bu and P. Feng, *Energy Environ. Sci.*, 2021, **14**, 1897–1927.

32 S. Zhao, Y. Wang, J. Dong, C.-T. He, H. Yin, P. An, K. Zhao, X. Zhang, C. Gao, L. Zhang, J. Lv, J. Wang, J. Zhang, A. M. Khattak, N. A. Khan, Z. Wei, J. Zhang, S. Liu, H. Zhao and Z. Tang, *Nat. Energy*, 2016, **1**, 16184.

This journal is © The Royal Society of Chemistry and IChemE 2023

Mol. Syst. Des. Eng., 2023, **8**, 1004–1012 | 1011

33 L. Zhuang, L. Ge, H. Liu, Z. Jiang, Y. Jia, Z. Li, D. Yang, R. K. Hocking, M. Li, L. Zhang, X. Wang, X. Yao and Z. Zhu, *Angew. Chem.*, 2019, **131**, 13699–13706.

34 B. Zhang, Y. Zheng, T. Ma, C. Yang, Y. Peng, Z. Zhou, M. Zhou, S. Li, Y. Wang and C. Cheng, *Adv. Mater.*, 2021, **33**, 2006042.

35 S. H. Eitel, M. Bauer, D. Schweinfurth, N. Deibel, B. Sarkar, H. Kelm, H.-J. Krüger, W. Frey and R. Peters, *J. Am. Chem. Soc.*, 2012, **134**, 4683–4693.

36 N. P. Cowieson, D. Aragao, M. Clift, D. J. Ericsson, C. Gee, S. J. Harrop, N. Mudie, S. Panjikar, J. R. Price, A. Riboldi-Tunnicliffe, R. Williamson and T. Caradoc-Davies, *J. Synchrotron Radiat.*, 2015, **22**, 187–190.

37 D. Aragao, J. Aishima, H. Cherukuvada, R. Clarken, M. Clift, N. P. Cowieson, D. J. Ericsson, C. L. Gee, S. Macedo, N. Mudie, S. Panjikar, J. R. Price, A. Riboldi-Tunnicliffe, R. Rostan, R. Williamson and T. T. Caradoc-Davies, *J. Synchrotron Radiat.*, 2018, **25**, 885–891.

38 W. Kabsch, *Acta Crystallogr., Sect. D: Biol. Crystallogr.*, 2010, **66**, 125–132.

39 G. Sheldrick, *Acta Crystallogr., Sect. C: Struct. Chem.*, 2015, **71**, 3–8.

40 G. M. Sheldrick, *Acta Crystallogr., Sect. A: Found. Crystallogr.*, 2008, **64**, 112–122.

41 O. V. Dolomanov, L. J. Bourhis, R. J. Gildea, J. A. K. Howard and H. Puschmann, *J. Appl. Crystallogr.*, 2009, **42**, 339–341.

42 A. L. Spek, *Acta Crystallogr., Sect. C: Struct. Chem.*, 2015, **71**, 9–18.

43 G. Ortiz, S. Brandes, Y. Rousselin and R. Guilard, *Chem. – Eur. J.*, 2011, **17**, 6689–6695.

44 S. Zhang, T. Yu, H. Wen, Z. Ni, Y. He, R. Guo, J. You and X. Liu, *Chem. Commun.*, 2020, **56**, 15387–15405.

45 K. N. Dinh, M. Chatti, T. D. Nguyen, D. A. Hoogeveen, D. R. MacFarlane and A. N. Simonov, *ACS Energy Lett.*, 2022, **7**, 3910–3916.

46 J. Xu, X. Zhu and X. Jia, *ACS Sustainable Chem. Eng.*, 2019, **7**, 16629–16639.

47 G. Beamson and D. Briggs, *J. Chem. Educ.*, 1993, **70**, A25.

48 C. V. Schenck, J. G. Dillard and J. W. Murray, *J. Colloid Interface Sci.*, 1983, **95**, 398–409.

49 N. R. Babij, E. O. McCusker, G. T. Whiteker, B. Canturk, N. Choy, L. C. Creemer, C. V. D. Amicis, N. M. Hewlett, P. L. Johnson, J. A. Knobelsdorf, F. Li, B. A. Lorsbach, B. M. Nugent, S. J. Ryan, M. R. Smith and Q. Yang, *Org. Process Res. Dev.*, 2016, **20**, 661–667.

50 M. C. Biesinger, B. P. Payne, A. P. Grosvenor, L. W. M. Lau, A. R. Gerson and R. S. C. Smart, *Appl. Surf. Sci.*, 2011, **257**, 2717–2730.

51 D. Wu, Y. Wei, X. Ren, X. Ji, Y. Liu, X. Guo, Z. Liu, A. M. Asiri, Q. Wei and X. Sun, *Adv. Mater.*, 2018, **30**, 1705366.

52 W. Zheng and L. Y. S. Lee, *ACS Energy Lett.*, 2021, **6**, 2838–2843.

1012 | *Mol. Syst. Des. Eng.*, 2023, **8**, 1004–1012

This journal is © The Royal Society of Chemistry and IChemE 2023